SCIENCE CHINA Materials ARTICLES

mater.scichina.com link.springer.com

Published online 20 July 2016 | doi: 10.1007/s40843-016-5067-4
Sci China Mater 2016, 59(7): 547–557

N,O-codoped porous carbon nanosheets for capacitors with ultra-high capacitance

Zhong Wu[1,2] and Xin-bo Zhang[1*]

ABSTRACT Significant enhancement of energy density of electrical double layered capacitors is a major challenge for electrochemical capacitors to conquer the emerging field of large scale renewable energy storage. The enhancement of specific capacitance is an effective strategy to obtain higher energy density. Addition of redox mediator in the electrolyte as pseudocapacitive sources could enhance the specific capacitance, but well-coupled electrode materials should be developed as well. Herein, as a proof-of-concept experiment, N, O-codoped porous carbon nanosheets have been fabricated, wherein graphene oxide is employed as both oxygen source as well as structure directing agent. Unexpectedly, the obtained electrode materials endow electrical double layered capacitors with excellent capacitive performances, including the ultra-high specific capacitance (5073.5 F g^{-1}) and excellent cycling stability, which could be attributed to the synergy of morphology and surface chemistry of N, O-codoped porous carbon nanosheets. These results would form the basis for an unprecedented perspective in the development of next generation electrode materials for electrical double layered capacitors.

Keywords: carbon nanosheets, redox mediator, capacitive performances

INTRODUCTION

Electrical double layer capacitors (EDLCs) have attracted numerous attentions as important electrochemical energy storage device due to their high power density, long cycle life, and low maintenance cost [1–3]. However, their further applications in other emerging fields such as large scale renewable energy storage are still hampered by their limited theoretical energy density [4–6]. To address this daunting challenge, many efforts have been devoted to improving the specific capacitance, as the energy density is proportional to the specific capacitance according to the equation: $E = 1/2CV^2$ (V is the applied potential window, and C is the specific capacitance) [7–9]. In response, one widely used strategy is to employ pseudocapacitive materials, which can improve the specific capacitance due to redox reactions of electrode materials, while the electrode materials themselves will be inevitably affected upon the redox reaction process, something like in rechargeable batteries [10–12]. Alternatively, addition of redox mediator in the electrolyte as pseudocapacitive sources could enhance the specific capacitance of EDLCs [13–16] and, more importantly, not necessarily compromise the excellent capacitive behaviors of electrode materials, because the Faradaic reactions occur in these redox-active electrolytes [17–21], keeping the electrode materials unaffected. Therefore, to exert the power of new redox electrolyte, development of well-coupled novel carbon materials to significantly improve the specific capacitance of EDLCs is of great importance [22–25].

Porous two-dimensional carbon nanosheets are of great interest as electrode materials for energy-storage devices due to their shortened paths for fast electrolyte ion diffusion and large accessible surface [26–29], offering more and fast electron/charge transfer channels [30–32]. In addition, functionalization of carbon materials, such as surface modification and heteroatom (N, O, etc.) doping, could further benefit the specific capacity by improving the electrolyte permeability, ion adsorbing, and so on [33–35]. Therefore, engineering the morphology and surface chemistry of carbon materials for EDLCs based on redox-active electrolyte is thus highly desirable while still very challenging [36–38].

In response, herein, as a proof-of-concept experiment, we first designed and demonstrated the synthesis of oxygen (O), nitrogen (N)-codoped porous carbon

[1] State Key Laboratory of Rare Earth Resource Utilization, Changchun Institute of Applied Chemistry, Chinese Academy of Sciences, Changchun 130022, China
[2] University of Chinese Academy of Sciences, Beijing 100049, China
[*] Corresponding author (email: xbzhang@ciac.ac.cn)

nanosheets derived from carbonization of graphene oxide (GO)@poly(benzoxazine-co-resol) by a facile and very effective route, wherein poly(benzoxazine-co-resol) was successfully polymerized from phenols, aldehydes, and diamines (nitrogen source). More importantly, GO was used in the reaction system to serve as both oxygen source and structure directing agent, which directed the *in situ* self-assembly of poly(benzoxazineco-resol) along the surface of GO. Interestingly, when the N, O-codoped porous carbon nanosheets (NOCPSs) used as an electrode material in EDLCs based on acidic (1 mol L^{-1} H_2SO_4) and redox-active electrolyte (0.09 mol L^{-1} $CuCl_2$ in 1 mol L^{-1} HNO_3), superior electrochemical performances were obtained, including the ultra-high specific capacitance of 5073.5 F g^{-1} and excellent cycling stability up to 4000 cycles.

EXPERIMENTAL SECTION

Materials

Graphite powders (325 mesh, Alfa Aesar, AR), potassium permanganate ($KMnO_4$, Aladdin Reagent, AR), sulphuric acid (H_2SO_4, Beijing Chemical Works, AR), phosphoric acid (H_3PO_4, Beijing Chemical Works, AR), hydrogen peroxide (H_2O_2, Aladdin Reagent, AR), hydrochloric acid (HCl, Beijing Chemical Works, AR), acetylene black (Hongxin Chemical Works), polyvinylidenefluoride (PVDF, DuPont Company, 99.9%), *N*-methyl-2-pyrrolidinone (NMP, Aladdin Reagent, AR), copper chloride ($CuCl_2$, Beijing Chemical Works, AR), nitric acid (HNO_3, Beijing Chemical Works, AR), formaldehyde (HCHO, Aladdin Reagent, AR), hydroquinone (HQ, Aladdin Reagent, AR), aniline (Beijing Chemical Works, AR), sodium dodecyl sulfate (Beijing Chemical Works, AR). Carbon paper was purchased from Torray. All reagents were used as received without any further purification.

Synthesis of GO

GO was prepared by the oxidation of natural graphite powder via an improved Hummers' method [39,40]. Briefly, a mixture of concentrated H_2SO_4/H_3PO_4 (45:5 mL/mL) was added to a mixture of graphite flakes (0.375 g) and $KMnO_4$ (2.25 g). The reaction mixture was then heated to 50°C and stirred for 24 h. The reaction was cooled to room temperature and poured onto ice (200 mL) with 30% H_2O_2 (3 mL). Then, the mixture was centrifuged (10,000 rpm for 5 min). The remaining solid material was then washed in succession with 200 mL of 30% HCl for twice, and 400 mL of water for three times. For each wash, the mixture was centrifuged (12,000 rpm for 10 min) and GO was obtained. The as-prepare GO was dispersed into deionized water to form a homogenous solution (about 1 mg mL^{-1}).

Preparation of NOPCSs

In a typical preparation process, a GO (4.5 mL, 1 wt.%) solution was dispersed in 30 mL deionized water by sonication for 4 h, and then 16 mg sodium dodecyl benzene sulfonate and 500 μL aniline was added into the solution. After stirring for 0.5 h, a resorcinol (120 mg)/formaldehyde solution (36 wt.%, 200 μL) was added. After another 0.5 h, the mixture was then transferred to 40 mL autoclave, sealed, and cured in an oven at 100°C for 24 h. A hydrogel was obtained and washed with excess distilled water. The water in the resulting gel was removed from the pores of the gel network by a freeze-drying technology. And then the sample NOPCSs was obtained after a carbonization process in a temperature-programmed furnace under an nitrogen flow, heated from room temperature to 800°C, and then kept at 800°C for 1 h and cooled down to room temperature.

Preparation of CNS

The sample CNS is synthesized by a similar procedure to the preparation of NOPCSs without involving GO. In brief, 16 mg sodium dodecyl benzene sulfonate and 500 μL aniline was added in 30 mL deionized water. After stirring for 0.5 h, a resorcinol (120 mg)/formaldehyde solution (36 wt.%, 200 μL) was added. After another 0.5 h, the mixture was then transferred to 40 mL autoclave, sealed, and cured in an oven at 100°C for 24 h. The as-prepared carbon precursor was washed with excess distilled water and then the water was removed by a freeze-drying technology. Finally, the sample CNS is obtained after a carbonization process at 800°C for 1 h under a nitrogen flow and cooled down to room temperature.

Materials characterization

X-ray diffraction (XRD) patterns were collected on Bruker D8 Focus Powder X-ray diffractometer using Cu Kα radiation (40 kV, 40 mA). The scanning electron microscopy (SEM) was performed by using a field emission scanning electron microscopy (FESEM, HITACHI, S-4800). Transmission electron microscopy (TEM), high-resolution TEM (HRTEM), scanning TEM (STEM) and energy dispersive X-ray (EDX) spectroscopy mapping technique were taken on an FEI Tecnai G2 electron microscope operated at 200 kV. X-ray photoelectron spectroscopy (XPS) measurements were performed on an ESCALAB 250 photoelectron spectrometer with monochromatic Al Kα X-rays. The specific surface area and porosity were determined by nitrogen

sorption using a Micrometritics ASAP 2020 analyzer. Specific surface areas were calculated by the Brunaure-Emmert-Teller (BET) method. Pore volumes and sizes were estimated from the pore size distribution curves from the adsorption isotherms using the Barrett-Joyner-Halenda (BJH) method. Fourier transform infrared spectroscopy (FTIR) was performed using a Thermo Nicolet 6700 spectrometer. Raman spectra were collected with a micro-Raman spectrometer (Renishaw) with a laser of 532 nm wavelength. The atomic force microscopy (AFM) was performed on Bruker Dimension Icon.

Electrochemical measurements

To evaluate the electrochemical properties of the as-prepared samples, working electrodes were prepared by mixing the as-prepared carbon nanomaterials (90 wt.%) as active materials and polyvinylidenefluoride (PVDF, 10 wt.%) as a binder. The mixtures were grounded in NMP and the obtained slurries were pasted onto a carbon paper substrate and then dried at 80°C overnight.

The electrochemical measurements were carried out using a three-electrode mode in 1 mol L^{-1} H_2SO_4 and 0.09 mol L^{-1} $CuCl_2$/1 mol L^{-1} HNO_3 aqueous solution. Ag/AgCl electrode filled with saturated KCl was used as reference electrode and a platinum plate was used as counter electrode. The sizes of all electrodes were fixed to ~2.0 cm×1.0 cm, and the average mass loading was ca. 1.0 mg. Electrochemical studies were carried out using VMP3 electrochemical workstation (Bio-logic Inc.) including cyclic voltammetry (CV), galvanostatic charge-discharge (GC) and electrochemical impedance spectroscopy (EIS). All the tests were performed at room temperature. Before testing, the electrode materials were activated for abundant cycles until they were stabilized at a certain condition. All the electrochemical measurements were done in 1 mol L^{-1} H_2SO_4 solution with a potential window of 1 V and in redox electrolyte with a potential window of 0.5 V. Typical CV and GC curves were measured at different scan rates and current densities, respectively. EIS tests were performed for the working electrode in a frequency range of 100 kHz–0.01 Hz at an open circuit potential with alternating current perturbation of 10 mV. The EIS data were analyzed using Nyquist plots, which represent the imaginary part (Z'') and real part (Z') of impedance.

RESULTS

The morphology and structure of the as-prepared samples were studied by FESEM and TEM. The synthesis of carbon nanosheets involves two main steps: polymerization and carbonization. At first, polymerization process was conducted through the hydrothermal method and novel three-dimensional hydrogel precursor, GO@poly(benzoxazineco-resol), was successfully formed (Fig. S1), wherein spherical poly(benzoxazineco-resol) was well anchored on the surface of GO (Fig. 1a). Followed by a carbonization process under the atmosphere of N_2, NOPCSs were obtained. The sheet-like morphology is illustrated in Figs 1b and c. The high-resolution TEM image of NOPCSs in Fig. 1d shows the carbon lattice with pores. For comparison, carbon materials derived from poly(benzoxazine-co-resol) without GO were synthesized through the same procedure, which are denoted as CNS.

Furthermore, the components and corresponding distribution in the NOPCSs were then analyzed using EDX spectroscopy mapping technique. The EDX spectrum in Fig. 1e illustrates the presence of C, N, and O in NOPCSs. It should be noted that N and O derived from the amide group in aniline and oxygen-containing functional groups in GO. Furthermore, the percentage of C, N and O in the sample was calculated after fitting the atom ratio corresponding to each element. The EDX data indicates that the material contains mainly C (97.37%) with a small amount of O (1.55%) and N (1.06%). Fig. 1f exhibits the STEM image of the NOPCSs. The sample NOPCSs was further characterized by element mapping images of C, O and N to analyze the elemental distribution as illustrated in Figs 1g–i. The distribution region of C (red dots), N (yellow dots), and O (green dots) is similar to the area in Fig. 1f. These results clearly show that the elements of C, N, and O are distributed homogeneously, further indicating uniform and complete doping process in the carbon skeleton. The introduction of heteroatom (N, O) can be used to tune the polarity of NOPCSs.

To examine the effect of GO on morphology and electrochemical properties, the similar process was conducted without the presence of GO. As shown in Figs S2a and b, the precursor poly(benzoxazineco-resol) was obtained after the hydrothermal process with the spherical morphology and the average diameter of 500 nm. After the carbonization treatment, the sample CNS was obtained and characterized by FESEM images as shown in Figs S2c and d. When there is no GO involved in the same procedures, the obtained CNS is observed as a thick blockbuster resulted from melting of poly(benzoxazineco-resol) during the carbonization process.

The pivotal step for the formation of carbon nanosheets is the presence of GO acting as anchoring agent and offering oxygen-containing functional groups. The rational structure design and synthesis of NOPCSs are of particular

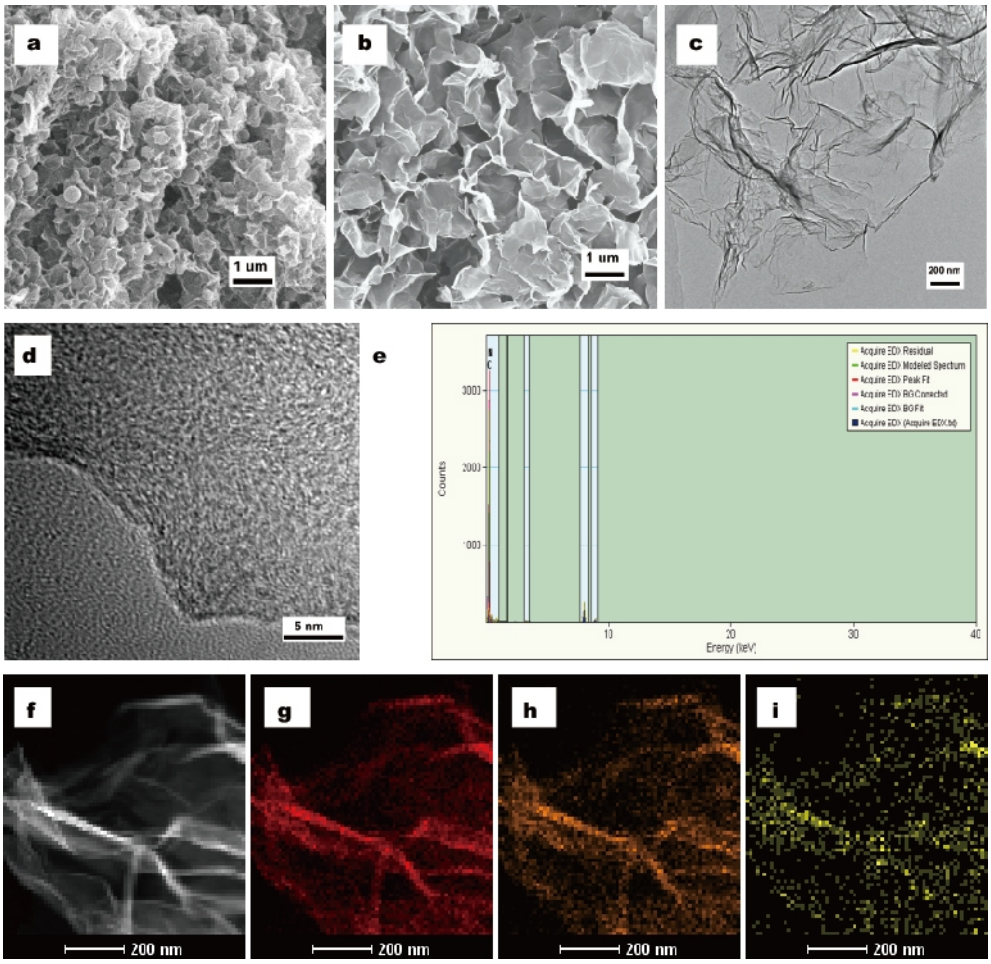

Figure 1 (a) FESEM image of the precursor GO@poly(benzoxazineco-resol). (b and c) FESEM and TEM images of NOPCSs. (d) HRTEM image of NOPCSs. (e) EDX spectrum of NOPCSs. (f) STEM image of NOPCSs and corresponding elemental mapping images of (g) C, (h) N and (i) O.

importance for advancing their applications. The thickness of NOPCSs sheet is characterized by AFM image as shown in Fig. S3. The average thickness is investigated as 8 nm.

As specific surface area and pore size might play an important role in electrochemical performance of carbon sheet, the N_2-adsorption-desorption isotherm and the pore-size distribution were collected as shown in Fig. 2a. The nitrogen adsorption-desorption isotherms of the sample NOPCSs can be categorized as being of type-II with a slight rise at low P/P_0 and a hysteresis loop at the high P/P_0 range of 0.4–1.0. The specific surface area of NOPCSs is found to be 351.455 $m^2\ g^{-1}$ by BET method.

The inset illustration in Fig. 2a is the corresponding pore diameter distribution curves, which is estimated by the BJH method using the isotherm adsorption branch. A total pore volume of the sample NOPCSs is found to be 0.822 $cm^3\ g^{-1}$. According to the pore-size distribution, it is clearly observed that mesopores with a wide size range (2–50 nm) are dominated in the composite, which may be constructed from the incompact stacking, entanglement and overlap of carbon nanosheets. The existence of abundant mesopores would facilitate the electrolyte diffusion to form a uniform interface between the electrode material and the electrolyte for the reversible redox processes and consequently result in enhanced electrochemical performances (vide infra). Importantly, the pore volume is dominated by mesopores including pore size around 3.8 nm with a narrow distribution and pore size ranging from 10 to 30 nm with a broad distribution. On one hand, the microporosity is accessible for the solvated electrolyte ions, providing higher capacitance at low charging rates. On the other hand, mesoporosity allows more electrolyte ion transportation in higher current densities, yielding higher rate capability. The presence of hierarchical porosity leads to the accessible surface area for electrolyte ions and suitable diffusion length. As a result, superior electrochemical perform-

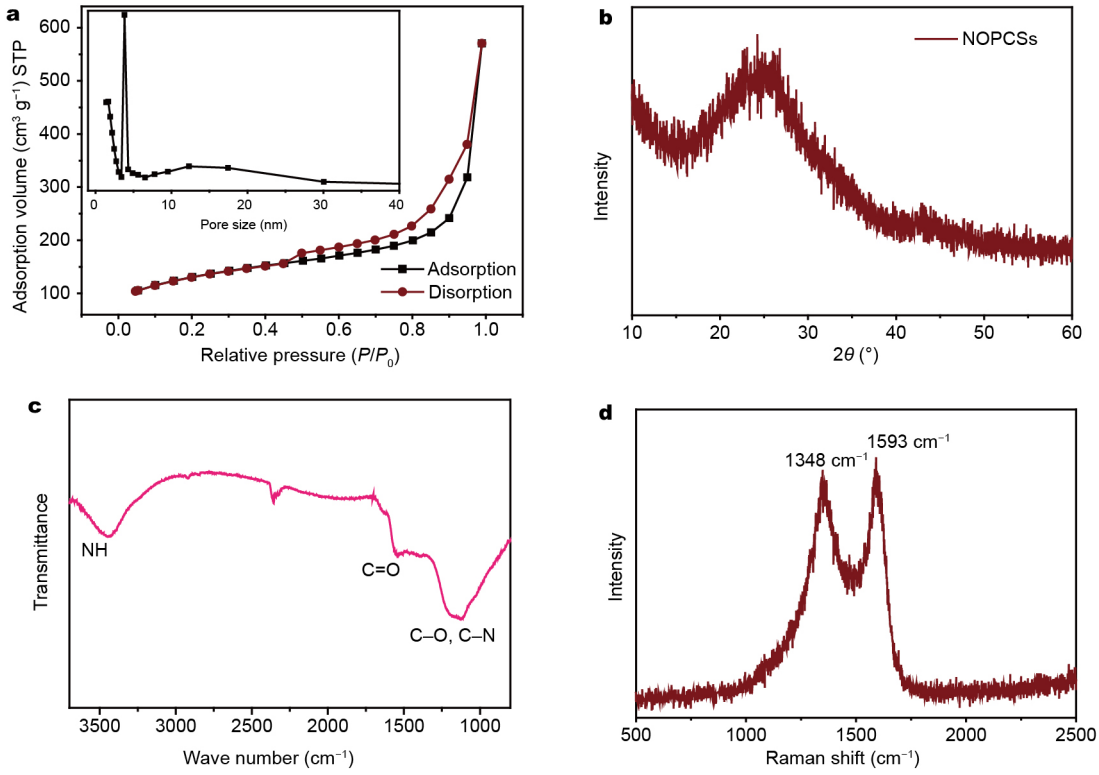

Figure 2 (a) Nitrogen adsorption-desorption isotherm and the pore-size distribution, (b) XRD pattern, (c) FTIR spectrum, and (d) Raman shift of the sample NOPCSs.

ances can be expected with enhanced specific capacitance.

To further characterize the sample NOPCSs, XRD was performed as shown in Fig. 2b. The XRD diffraction spectra of NOPCSs shows a broad diffraction peaks positioned at 2θ angle of about 26°, which can be indexed to the (002) plane of graphitic carbon (JCPDS 75-1621). The broadening peak suggests the existence of carbon sheets. FTIR yields more meaningful spectra for functional groups and is used to confirm the presence of chemical interaction/bonding. Fig. 2c illustrates FTIR spectra for the sample NOPCSs, exhibiting the presence of NH, C=O, C–O and C–N bonds. Intense peaks observed at 1150 cm^{-1} in the sample were attributed to stretching of the C–O and C–N bonds. The presence of multiple peaks at 1720 cm^{-1} is due to overlap of the carbonyl (C=O) bonds. The Raman spectrum of the sample NOPCSs is presented in Fig. 2d, which illustrates the characteristics representative of disordered carbon. The peak positioned at 1593 cm^{-1} corresponds to the G band, which is attributed to amorphous sp^2-bonded forms of carbon. The D-band located at approximately 1348 cm^{-1} is attributed to the defect-induced structure resulted from dopants and functional groups. The broad peak of D band in our work implies the nitrogen dopants and oxygen functional groups. These results demonstrate the formation of carbon nanosheets with structural defects with nitrogen dopants and oxygen-functional groups in our work.

XPS technique was conducted to further analyze the chemical state of all elements in the sample NOPCSs. The XPS spectrum presented in Fig. 3a clearly indicates the presence of C, N and O, which is consistent with the EDX results in Fig. 1e. Further studies are needed to be carried out to ascertain the bonding configurations of these atoms by high resolution XPS spectra. The high resolution C 1s spectra are presented in Fig. 3b, which show peaks at four binding energies. The characteristic intense peak at 284.5 ± 0.1 eV is mainly due to carbon atoms attached to C–C bond. Peaks at higher binding energies suggest the presence of oxidized carbon atoms, C=O at 288.8 ± 0.1 eV, C–O at 286.4 ± 0.1 eV and C–N/C=C at 285.4 ± 0.1 eV. From the de-convoluted peak of N 1s spectra in Fig. 3c, we can conclude that the sample NOPCSs is doped by three types of nitrogen-containing groups, namely, pyridinic-N species (N-6, 397.2 ± 0.1 eV), pyrrolic-N (N-5, 400.0 ± 0.1 eV) and pyridine-N-oxide (N-X, 405.1 ± 0.1 eV). The de-convoluted peaks of oxygen are revealed in Fig. 3d.

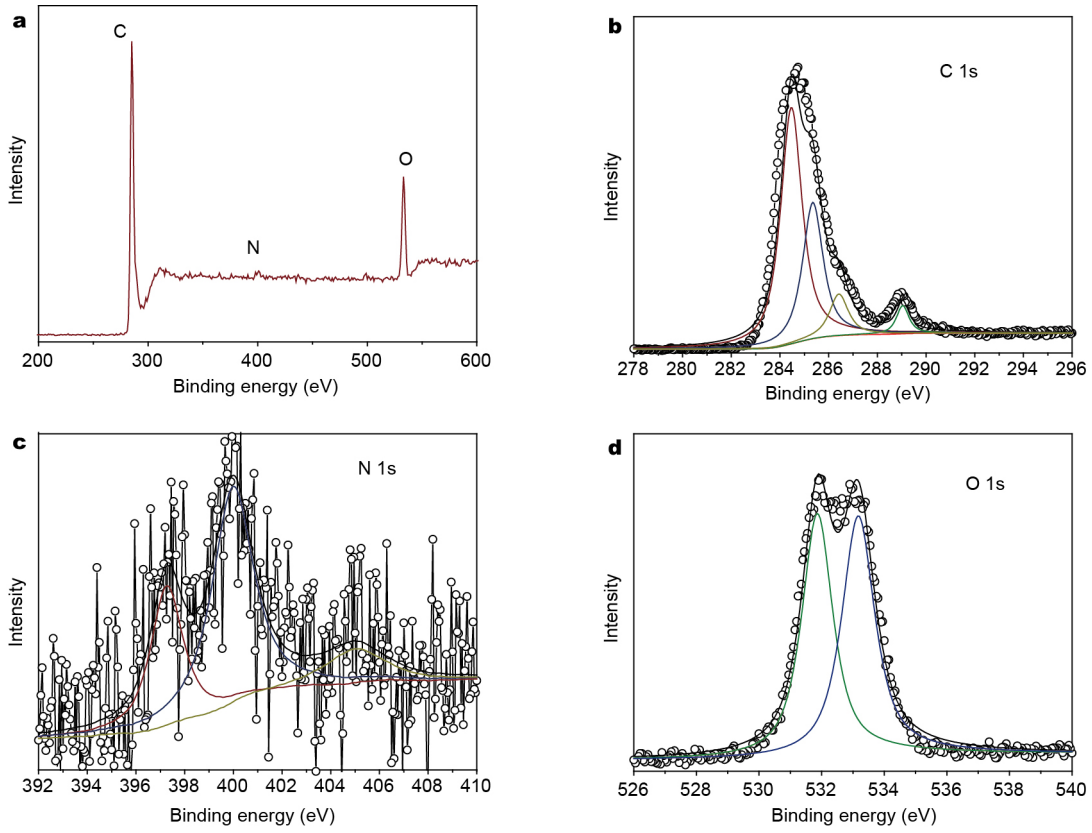

Figure 3 (a) The survey XPS spectrum, (b) deconvolution of C 1s spectrum, (c) deconvolution of N 1s spectrum, and (d) deconvolution of O 1s spectrum of the sample NOPCSs.

There are two peaks in the O 1s spectra positioned at the binding energies of 531.9 and 533.2 eV, which are correspond to C=O and O–C=O, respectively. These results demonstrate the effective nitrogen dopants and oxygen-containing functional groups in carbon nanosheets. The presence of N and O enables the sample NOPCSs more hydrophilic and readily dispersed in aqueous solution. The surface chemistry will greatly affect their electrochemical behaviors.

To evaluate the advantages of the as-prepared materials and their potential applications as electrodes for supercapacitors (SCs), the electrochemical performances of those electrodes were measured in 1 mol L^{-1} H_2SO_4 and 0.09 mol L^{-1} $CuCl_2$ in 1 mol L^{-1} HNO_3 aqueous solution electrolyte. At first, the synthesized samples were tested as electrode materials for EDLCs in 1 mol L^{-1} H_2SO_4. Fig. 4a shows the CV curves of NOPCSs and CNS at the scan rate of 20 mV s^{-1} between 0 and 1 V. The nearly rectangular-like shape shows the capacitive behavior with EDLCs-based charge storage mechanism. It is worth noting that the specific capacitance of NOPCSs is 107.2 F g^{-1}, which is much higher than that of CNS with the specific capacitance of 2.64 F g^{-1}. Fig. S5a illustrates the CV curves of NOPCSs over a wide range of scan rates ranging from 2 to 500 mV s^{-1}. Even at a high scan rate of 500 mV s^{-1}, the CV curve also retains a stable rectangular shape with no obvious distortion indicating a remarkable rate capability.

The specific capacitance (C_s, F g^{-1}) values at various scan rates (mV s^{-1}) in the CV measurements were calculated using the following equation [41,42]:

$$C_s = \frac{\oint I\mathrm{d}V}{2\omega v \Delta V},$$

where ΔV (V) is the applied potential window, v is the scan rate, and w (g) is the weight of the active material. The specific capacitances of NOPCSs and CNS at various scan rates are illustrated in Table S1 (Supplementary information). In brief, the highest specific capacitance of NOPCSs is 120.3 F g^{-1} at 2 mV s^{-1}. Even at the high scan rate of 50 mV s^{-1}, the specific capacitance of NOPCSs is still 103.0 F g^{-1}, indicating its excellent rate capability.

For comparison with NOPCSs, the capacitive performances of CNS were also measured (Fig. S6 and Table S1)

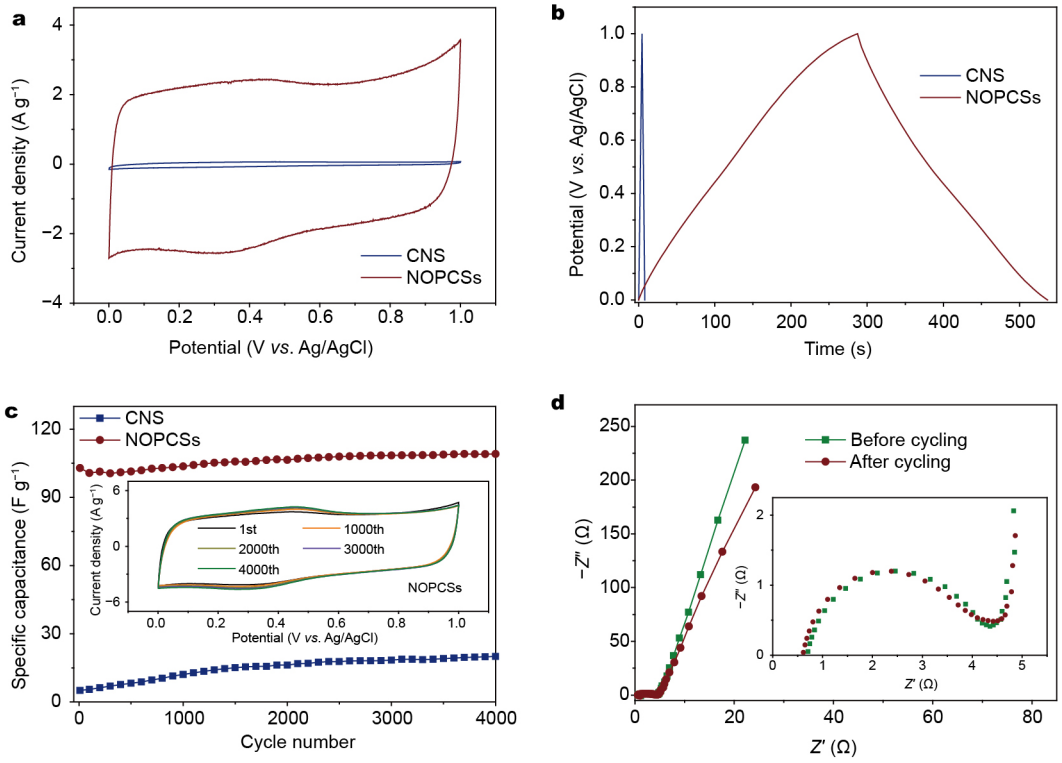

Figure 4 Electrochemical measurements in 1 mol L^{-1} H_2SO_4. (a) CV curves of NOPCSs and CNS at a scan rate of 20 mV s^{-1}. (b) GC curves of NOPCSs and CNS at a current density of 0.5 A g^{-1}. (c) Cycling stability of NOPCSS and CNS at 50 mV s^{-1}. Inset is the CV curves of NOPCSs at 1st, 1000th, 2000th, 3000th and 4000th cycle. (d) EIS data of NOPCSs before and after 4000 cycles. Inset is the enlarged plots.

—only very limited specific capacitances below 10 F g^{-1} are obtained. Besides, GC measurements were performed to clarify the charge storage mechanism and specific capacitance calculation. Fig. 4b shows the GC curves of NOPCSs and CNS at the current density of 0.5 A g^{-1}. The symmetrical triangular charge/discharge characteristics and a quick *I*-*V* response confirm the ideal EDLCs behavior of NOPCSs and CNS. However, better capacitor performances of NOPCSs have been revealed, which is in accordance with the results of CV curves.

From the materials structure perspective, superior electrochemical performances are contributed to the unique structure of NOPCSs. Firstly, the nanosheets structure is favorable for double layer formation at the electrode-electrolyte interface. Secondly, hierarchical pore structures allow more effective ion transportation and short diffusion length for higher specific capacitance. The porosity of NOPCSs is composed of micropores with the average pore size of 3.8 nm and mesopores ranging from 10 to 30 nm. The pore size is higher than the electrolyte ion sizes of 0.42 nm and 0.53 nm for solvated cation (H_3O^+) and anion (SO_4^{2-}) in H_2SO_4 solution respectively. In contrast, there is no obvious pore involving in CNS. Consequently, the sample NOPCSs shows superior properties with low equivalent series resistance and fast diffusion of ions from electrolyte into the sample.

For practical application, cyclic stability is crucial for an electrode material to be used in SCs. In this context, we performed CV tests for 4000 times between 0 and 1 V at the scan rate of 50 mV s^{-1}. The CV curves as a function of cycle number is plotted in Fig. 4c. An increase can be found before 1000 cycles, which may be attributed to the improvement of ion accessibility. There is no obvious degradation after 4000 cycles indicating their good cycling stability, which is confirmed by the CV curves of NOPCSs at 1st, 1000th, 2000th, 3000th and 4000th cycle. These advanced properties ensure the NOPCSs a great promise as an electrode material for EDLCs.

To further analyze the detailed characteristics of NOPCSs, EIS was performed in the frequency range of 10 mHz–10 kHz with a signal amplitude of 10 mV. EIS spectra investigated the transport characteristics of the charge carriers within electrode using a Nyquist plot, which represents the imaginary part ($-Z''$) and real part (Z') of impedance. The impedance spectra consist of one semicircle at high frequency, followed by a straight line at

the low frequency range. The high frequency semicircle intercepts the real axis at R_s and (R_s + R_{ct}), while R_s means a bulk solution resistance and R_{ct} means a charge-transfer resistance, respectively. The Nyquist plot expanded in the high frequency region is given in the inset. Fig. 4d shows Nyquist plot of NOPCSs as capacitive electrode. The R_s value is about 0.7 and 0.63 Ω before and after cycling, respectively. R_{ct} is about 1.84 and 1.95 Ω before and after cycling calculated on the basis of the radius of the semicircle. In terms of R_s and R_{ct}, we can note that there is no obvious distinction for NOPCSs electrodes before and after cycling, which is accordance with their good cycling stability. The inclined portion of the curve in the low frequency is ascribed to the Warburg impedance, which is related to ion diffusion/transport in the electrolyte. The vertical nature of the Nyquist plots clearly indicates the capacitive behavior of the material. The more vertical shape at low frequency for NOPCSs electrodes before cycling indicates a more capacitive behavior of the electrode.

DISCUSSION

In order to increase the specific capacitance, redox-active electrolyte is also employed as electrolyte. In our work, the redox-active electrolyte is fabricated by incorporating 0.09 mol L^{-1} $CuCl_2$ into 1 mol L^{-1} HNO_3 electrolyte. $CuCl_2$ is selected as redox mediators because it can efficiently fix the position of the C–O bond on the surface and reducing $CuCl_2$ in the electrolyte can then generate an additional redox CuCl layer as follows: $CuCl_2 + C{=}O^+ e^- \rightarrow CuClCO_{surface\ layer} + Cl^-$ [25].

The CV curves of NOPCSs in redox-active electrolyte are illustrated in Fig. 5a. The important change happens in terms of the shape of CV curves because of the introduction of redox-active additives. A pair of peaks are observed at 0.34 and 0.07 V, indicating their pseudocapacitive behavior resulted from the redox-active electrolyte. The CV curves of NOPCSs and CNS reveal their similar charge storage mechanism and the superior specific capacitance of NOPCSs to that of CNS at the scan rate of 20 mV s^{-1}.

Fig. 5b presents the correlation between the specific capacitance and the various scan rates for the samples NOPCSs and CNS. The highest specific capacitance of 5073.5 F g^{-1} is achieved for the sample NOPCSs at the scan rate of 2 mV s^{-1}, which is near 15-fold higher than that of

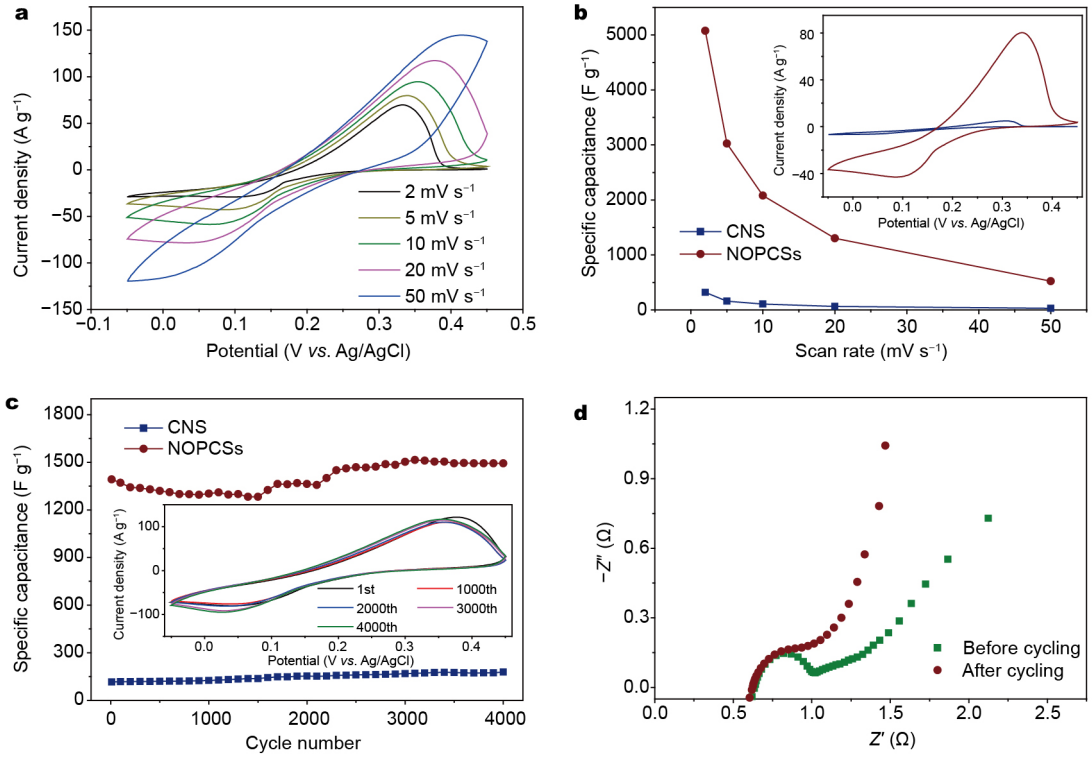

Figure 5 Electrochemical measurements in the redox-active electrolyte (0.09 mol L^{-1} $CuCl_2$ + 1 mol L^{-1} HNO_3). (a) CV curves of the NOPCSs at various scan rates. (b) The variation of specific capacitances with scan rates of NOPCSs and CNS. (Inset plots are CV curves of NOPCSs and CNS at the scan rate of 20 mV s^{-1}). (c) Cycling stability of NOPCSs and CNS at 20 mV s^{-1}. Inset plots are CV curves of NOPCSs at 1st, 1000th, 2000th, 3000th and 4000th cycle. (d) EIS data of NOPCSs before and after 4000 cycles.

Table 1 A detailed comparison of the highest specific capacitance of NOPCSs with literatures

Electrode materials	Specific capacitance	Electrolyte	Ref.
Reduced graphene oxide hydrogels	252.6 F g^{-1} at 1 A g^{-1}	H_2SO_4 + hydroquinone	[21]
Polyaniline-coated graphene	553 F g^{-1} at 1 A g^{-1}	H_2SO_4 + hydroquinone	[22]
Activated carbons	630.6 F g^{-1} at 1 mA cm^{-2}	$VOSO_4$ + 1 mol L^{-1} H_2SO_4	[23]
Activated carbons	912 F g^{-1} at 2 mA cm^{-2}	0.08 mol L^{-1} KI + 1 mol L^{-1} H_2SO_4	[24]
Surface-functionalized, porous carbon	4700 F g^{-1} at 5 mV s^{-1}	0.09 mol L^{-1} $CuCl_2$ + 1 mol L^{-1} HNO_3	[25]
N, O-codoped porous carbon nanosheets	5073.5 F g^{-1} at 2 mV s^{-1}	0.09 mol L^{-1} $CuCl_2$ + 1 mol L^{-1} HNO_3	Our work

the CNS (319.5 F g^{-1}). For comparison, Table S2 summarizes the specific capacitances of NOPCSs and CNS calculated from CV curves in $CuCl_2/HNO_3$ redox-active electrolyte, which is illustrated in supporting information. It is found that the specific capacitances of CNS are much lower than those of the NOPCSs at all tested conditions, providing another evidence for the superiority of the NOPCSs. Table 1 lists a detailed comparison on their high specific capacitance with previous literatures.

Moreover, the sample NOPCSs in redox-active electrolyte is 50-fold enhancement in the specific capacitance compared with previous results in acidic electrolyte. The functional groups of NOPCSs offer tremendous opportunities for carbon nanomaterials with desired properties, which are evidenced by FTIR and XPS measurements. Discussing the impact of their functional groups on the pseudocapacitive behaviors, this increase is resulted from the reaction of $CuCl_2$ with carbonyl groups at the surface of NOPCSs. These results further demonstrate that the addition of redox additive is compatible with active electrode materials and enhanced specific capacitance can be achieved through the introduction of redox-active electrolyte.

To investigate the cycling stability, CV tests were performed for 4000 times between –0.05 and 0.45 V at 20 mV s^{-1}. The CV curves as a function of cycle number is plotted in Fig. 5c. The sample CNS is stable in redox-active electrolyte due to their limited specific capacitance. The sample NOPCSs exhibits excellent cycling stability after 4000 cycles. However, the cycling stability of NOPCSs is shifting until 2500 cycles. The inset plots in Fig. 5c shows the corresponding CV curves of NOPCSs at 1^{st}, 1000^{th}, 2000^{th}, 3000^{th} and 4000^{th} cycle. After 4000 cycles, the specific capacitance of NOPCSs is stable at 1493.2 F g^{-1}.

Aforementioned results are also supported by EIS analysis, which investigates the transfer characteristics of NOPCSs during the cycling tests. Fig. 5d illustrates the EIS spectra of NOPCSs before and after cycling. In the high-frequency region, the real axis intercept is the equivalent series resistance (ESR), and the width of semicircle plotted is indicative of the charge-transfer resistance in the electrode materials. The ESR value is near 0.62 Ω. Moreover, the semicircle observed in the high frequency range corresponds to the charge transfer resistance caused by Faradic reactions. The obtained charge transfer resistances are about 0.19 and 0.21 Ω before and after cycling, respectively, which shows negligible change for mass transfer resistance and internal cell resistance. Compared to conventional SCs, the SCs using redox-active electrolyte exhibit a shorter Warburg-type line and smaller diameter arc. These results demonstrate a lower charge transfer resistance and more efficient electrolyte diffusion.

CONCLUSIONS

In conclusion, as a proof-of-concept experiment, to exert the power of new redox electrolyte by developing well-coupled novel carbon materials, we developed and demonstrated a facile while effective "hitting three birds with one stone" strategy to fabricate N, O-codoped porous carbon nanosheets, wherein GO is employed as both oxygen source as well as structure directing agent. Unexpectedly, when first employed as novel electrode material in EDLCs based on redox-active electrolyte, excellent electrochemical performances have been obtained, including the ultra-high specific capacitance of 5073.5 F g^{-1} and excellent cycling stability up to 4000 cycles.

Received 10 May 2016; accepted 15 June 2016; published online 20 July 2016

1 Burt R, Birkett G, Zhao XS. A review of molecular modelling of electric double layer capacitors. Phys Chem Chem Phys, 2014, 16: 6519–6538
2 Chen S, Liu Y, Chen J. Heterogeneous electron transfer at nanoscopic electrodes: importance of electronic structures and electric double layers. Chem Soc Rev, 2014, 43: 5372–5386
3 Zhai Y, Dou Y, Zhao D, *et al.* Carbon materials for chemical capacitive energy storage. Adv Mater, 2011, 23: 4828–4850
4 Simon P, Gogotsi Y. Materials for electrochemical capacitors. Nat Mater, 2008, 7: 845–854
5 Sahu V, Shekhar S, Sharma RK, *et al.* Ultrahigh performance supercapacitor from lacey reduced graphene oxide nanoribbons. ACS

Appl Mater Interfaces, 2015, 7: 3110–3116
6 Choi NS, Chen Z, Freunberger SA, *et al.* Challenges facing lithium batteries and electrical double-layer capacitors. Angew Chem Int Ed, 2012, 51: 9994–10024
7 Yang Z, Ren J, Zhang Z, *et al.* Recent advancement of nanostructured carbon for energy applications. Chem Rev, 2015, 115: 5159–5223
8 Biswal M, Banerjee A, Deo M, *et al.* From dead leaves to high energy density supercapacitors. Energy Environ Sci, 2013, 6: 1249–1259
9 Cai J, Niu H, Li Z, *et al.* High-performance supercapacitor electrode materials from cellulose-derived carbon nanofibers. ACS Appl Mater Interfaces, 2015, 7: 14946–14953
10 Wu Z, Huang XL, Wang ZL, *et al.* Electrostatic induced stretch growth of homogeneous β-Ni(OH)$_2$ on graphene with enhanced high-rate cycling for supercapacitors. Sci Rep, 2014, 4: 3669
11 Chen H, Zhou S, Wu L. Porous nickel hydroxide–manganese dioxide-reduced graphene oxide ternary hybrid spheres as excellent supercapacitor electrode materials. ACS Appl Mater Interfaces, 2014, 6: 8621–8630
12 Augustyn V, Simon P, Dunn B. Pseudocapacitive oxide materials for high-rate electrochemical energy storage. Energy Environ Sci, 2014, 7: 1597–1614
13 Zhong C, Deng Y, Hu W, *et al.* A review of electrolyte materials and compositions for electrochemical supercapacitors. Chem Soc Rev, 2015, 44: 7484–7539
14 Senthilkumar ST, Selvan RK, Melo JS. Redox additive/active electrolytes: a novel approach to enhance the performance of supercapacitors. J Mater Chem A, 2013, 1: 12386–12394
15 Han S, Wu D, Li S, *et al.* Porous graphene materials for advanced electrochemical energy storage and conversion devices. Adv Mater, 2014, 26: 849–864
16 Qian W, Sun F, Xu Y, *et al.* Human hair-derived carbon flakes for electrochemical supercapacitors. Energy Environ Sci, 2014, 7: 379–386
17 Roldán S, Granda M, Menéndez R, *et al.* Mechanisms of energy storage in carbon-based supercapacitors modified with a quinoid redox-active electrolyte. J Phys Chem C, 2011, 115: 17606–17611
18 Akinwolemiwa B, Peng C, Chen GZ. Redox electrolytes in supercapacitors. J Electrochemical Soc, 2015, 162: A5054–A5059
19 Chen L, Bai H, Huang Z, *et al.* Mechanism investigation and suppression of self-discharge in active electrolyte enhanced supercapacitors. Energy Environ Sci, 2014, 7: 1750–1759
20 Roldán S, Blanco C, Granda M, *et al.* Towards a further generation of high-energy carbon-based capacitors by using redox-active electrolytes. Angew Chem Int Ed, 2011, 50: 1699–1701
21 Pham VH, Gebre T, Dickerson JH. Facile electrodeposition of reduced graphene oxide hydrogels for high-performance supercapacitors. Nanoscale, 2015, 7: 5947–5950
22 Chen W, Rakhi RB, Alshareef HN. Capacitance enhancement of polyaniline coated curved-graphene supercapacitors in a redox-active electrolyte. Nanoscale, 2013, 5: 4134–4138
23 Senthilkumar ST, Selvan RK, Ponpandian N, *et al.* Improved performance of electric double layer capacitor using redox additive (VO^{2+}/VO_2^+) aqueous electrolyte. J Mater Chem A, 2013, 1: 7913–7919
24 Senthilkumar ST, Selvan RK, Lee YS, *et al.* Electric double layer capacitor and its improved specific capacitance using redox additive electrolyte. J Mater Chem A, 2013, 1: 1086–1095
25 Mai LQ, Minhas-khan A, Tian X, *et al.* Synergistic interaction between redox-active electrolyte and binder-free functionalized carbon for ultrahigh supercapacitor performance. Nat Commun, 2013, 4: 2923
26 Fan H, Shen W. Carbon nanosheets: synthesis and application. ChemSusChem, 2015, 8: 2004–2027
27 Huang J, Wang J, Wang C, *et al.* Hierarchical porous graphene carbon-based supercapacitors. Chem Mater, 2015, 27: 2107–2113
28 Liu J, Wickramaratne NP, Qiao SZ, *et al.* Molecular-based design and emerging applications of nanoporous carbon spheres. Nat Mater, 2015, 14: 763–774
29 Amali AJ, Sun JK, Xu Q. From assembled metal–organic framework nanoparticles to hierarchically porous carbon for electrochemical energy storage. Chem Commun, 2014, 50: 1519–1522
30 Zhang C, Lv W, Tao Y, *et al.* Towards superior volumetric performance: design and preparation of novel carbon materials for energy storage. Energy Environ Sci, 2015, 8: 1390–1403
31 Zheng X, Luo J, Lv W, *et al.* Two-dimensional porous carbon: synthesis and ion-transport properties. Adv Mater, 2015, 27: 5388–5395
32 Es-souni M, Schopf D. Modified nanocarbon surfaces for high performance supercapacitor and electrocatalysis applications. Chem Commun, 2015, 51: 13650–13653
33 Hasegawa G, Deguchi T, Kanamori K, *et al.* High-level doping of nitrogen, phosphorus, and sulfur into activated carbon monoliths and their electrochemical capacitances. Chem Mater, 2015, 27: 4703–4712
34 Wu ZS, Parvez K, Winter A, *et al.* Layer-by-layer assembled heteroatom-doped graphene films with ultrahigh volumetric capacitance and rate capability for micro-supercapacitors. Adv Mater, 2014, 26: 4552–4558
35 Li B, Dai F, Xiao Q, *et al.* Nitrogen-doped activated carbon for a high energy hybrid supercapacitor. Energy Environ Sci, 2016, 9: 102–106
36 Hao GP, Li WC, Qian D, *et al.* Structurally designed synthesis of mechanically stable poly(benzoxazine-co-resol)-based porous carbon monoliths and their application as high-performance CO_2 capture sorbents. J Am Chem Soc, 2011, 133: 11378–11388
37 Hao GP, Lu AH, Dong W, *et al.* Sandwich-type microporous carbon nanosheets for enhanced supercapacitor performance. Adv Energy Mater, 2013, 3: 1421–1427
38 Guo DC, Mi J, Hao GP, *et al.* Ionic liquid $C_{16}mimBF_4$ assisted synthesis of poly(benzoxazine-co-resol)-based hierarchically porous carbons with superior performance in supercapacitors. Energy Environ Sci, 2013, 6: 652–659
39 Hummers WS, Offeman RE. Preparation of graphitic oxide. J Am Chem Soc, 1958, 80: 1339–1339
40 Marcano DC, Kosynkin DV, Berlin JM, *et al.* Improved synthesis of graphene oxide. ACS Nano, 2010, 4: 4806–4814
41 Zhu Y, Murali S, Stoller MD, *et al.* Carbon-based supercapacitors produced by activation of graphene. Science, 2011, 332: 1537–1541
42 Wang H, Casalongue HS, Liang Y, *et al.* Ni(OH)$_2$ nanoplates grown on graphene as advanced electrochemical pseudocapacitor materials. J Am Chem Soc, 2010, 132: 7472–7477

Acknowledgments This work was supported by the National Natural Science Foundation of China (51471075, 51401084 and 51101070).

Author contributions Wu Z carried out the experiments and wrote the paper. Zhang XB supervised the research and revised the manuscript. All authors reviewed the manuscript.

Conflict of interest The authors declare that they have no conflict of interest.

Supplementary information Supporting data are available in the online version of the paper.

Zhong Wu received her BSc degree from the College of Chemistry and Materials Science, Anhui Normal University in 2010. She obtained her PhD degree under the direction of Prof. Xinbo Zhang at Changchun Institute of Applied Chemistry (CIAC), Chinese Academy of Sciences (CAS) in 2016. Her research interests focus on the synthesis and characterization of advanced inorganic nanomaterials, especially metal-oxide and carbon-based materials and their application in supercapacitors.

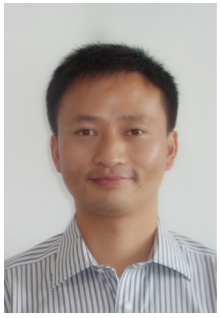

Xinbo Zhang is a full professor at CIAC, CAS. He obtained his PhD in inorganic chemistry from CIAC, CAS in 2005. From 2005–2009, he worked as a Japan Society for the Promotion of Science (JSPS) postdoctoral fellow (2005–2007) and a the New Energy and Industrial Technology Development Organization (NEDO) research associate (2007–2009) at the National Institute of Advanced Industrial Science and Technology (AIST), Japan. His interests mainly focus on functional inorganic materials for batteries, fuel cells, electrochemical water splitting and carbon dioxide reduction. He has published over 70 peer-reviewed articles, including *Nat Commun, JACS, Angew Chem Int Ed, Adv Mater, Chem Soc Rev, Energy Environ Sci,* with more than 5000 citations and H-index of 40. He also holds or has filed over 20 patents and patent applications. Selected awards include "Hundred Talents Program" of CAS (2011), the Excellent Young Scholars of NSFC (2014), and Young Top-Notch Talent (2015).

氮氧共掺杂多孔碳片用于超高比容量的超级电容器

吴中[1,2], 张新波[1*]

摘要 如何有效提升双层电容器的能量密度是一个亟待解决的重大课题, 而提高其比容量是其中一种有效提高能量密度的常用方法. 与常见的加入赝电容材料的方法不同, 本论文通过在电解液中加入氧化还原介质的方法达到提升比容量的目的. 在这一方法中, 得到显著提高的比容量主要来源于氧化还原介质贡献的氧化还原行为. 这一方法的优异之处在于氧化还原反应是发生在电解液中而非电极材料上, 因此在一定程度上保证了电极材料的稳定性. 在电极材料的设计上, 通过简便的方法制备得到了氮氧共掺杂多孔碳片. 在这一合成过程中, 氧化石墨不仅可以提供氧实现杂原子掺杂, 而且它的二维片状结构可以作为模板诱导碳片的形成. 经制备的碳材料在氧化还原电解液体系中获得了优异的电化学性能, 尤其表现在它超高的比容量(5073.5 F g^{-1}). 这一优异的电化学性能得益于碳片材料独特的形貌结构、表面特征以及它与电解液之间的相互作用. 本文中使用氧化还原介质来提升比容量的方法为高性能双电层电容器的设计提供了新的方向.